# DRDC | RDDC

Metamaterial designs for photovoltaic and IR focal-plane-imaging array applications

Prepared by:
M. Memarian and G.V. Eleftheriades
Department of Electrical and Computer Engineering
University of Toronto
172 St George St, Toronto, ON M5R 0A3

Defence Research and Development Canada

Canada

The Edward S. Rogers Sr. Department
of Electrical & Computer Engineering
UNIVERSITY OF TORONTO

Metamaterial Designs For Photovoltaic and IR Focal-Plane-Imaging Array Applications

Prepared for

Defence Research and Development Canada (DRDC)

Prepared by

M. Memarian

G.V. Eleftheriades

13 March 2013

Abstract

In this work we propose several designs and techniques for collecting, refracting and guiding an incoming electromagnetic wave in the lightwave regime. We primarily make use of low permittivity anisotropic media synthesized using bilayers of plasmonic metal and dielectric. By devising hetero-junctions from a combination of rotated versions of these metamaterial media, we propose ways to concentrate light either inside the structure, or focus the power outside. Physical realizations at the optical/IR regimes are presented. The proposed designs are shown to be applicable to various scenarios including photo- and thermo-voltaics, photo-detectors, sensors and focal-plane-imaging arrays (FPAs), and optical antennas. The specific issue of power loss in FPAs is addressed using these devices.

Table of Contents

List of Figures

1 Introduction

In this work we propose metamaterial (MTM) structures and designs, specifically using low-index anisotropic metamaterials, for focusing, guiding, absorption, emission, and collimation of visible and/or Infra-red light to enable applications in solar and/or thermo-photovoltaic structures, photo-detectors, and infrared focal plane arrays. This work can be further used in the areas of non-imaging optics, illumination optics, and as alternatives to micro and nano Fresnel lenses.

1.1 Photovoltaic and Thermophotovoltaic Applications

In the first part of this project, we extensively studied the literature on several concepts related to Photovoltaics [1]-[24], and investigated possible novel MTM designs pertaining to these various applications.

A potentially practical use of periodic structures and metamaterials is in solar cell applications, especially for the design of solar concentrators, thermal absorbers, and emitters. Concentrated photovoltaics (CPV) is an area of research which aims to reduce the overall cost of the system by using smaller number of PV cells. The idea is to collect sunlight over a larger surface area, concentrate it into a smaller area and shine it on to a PV. This results in using less PV cells per overall area, which makes this solution much more economically viable. For this purpose, several techniques have been used up to now such as reflectors, refractors including Fresnel lenses, hybrid methods, luminescent and fluorescent structures, which all have their respective advantages and disadvantages in practice [1]. Techniques such as dichroic dispersion have also been reported, where the wideband light is split into different wavelength regimes, and shined on different solar cells each tuned to that color of light. Some of the key aspects required for a CPV system is low loss, high concentration, low profile, low cost, and angle independence from incident radiation [1]. A suggestion of using metamaterials in this area has been proposed in [22].

Metamaterials have been more recently explored in the area of Thermo-photovoltaics (TPV). In this application, an emitter is heated, through burning of fuel or other means. The emitter has a certain operating wavelength (or emission bandwidth) over the Infrared (IR) range, such that it emits IR radiation that matches the bandgap of a Thermal PV cell (TPV), where the photocurrent is produced. A system that uses energy from solar radiation for heating the TPV emitter is known as a Solar thermo-photovoltaic (STPV) system, which has been proposed in works as early as

[17]. In STPV systems, sunlight (solar radiation) is absorbed by a layer that is highly absorptive, has low reflections, and preferably operates over a wideband to absorb all wavelengths of solar radiation. The energy dissipated in the absorber causes an increase in temperature, which in turn heats up a thermal emitter with the requirements discussed.

The research involving usage of metamaterials in solar and TPV applications can be divided as follows. Significant effort has been placed in the design of perfect absorbers using MTMs [2]-[8], while some researchers have focused on the design of emitters [9]- [16], and a few works have demonstrated STPV [17]- [19] systems, such as the SANTE (Solar Absorber Narrow Band emitter) proposed in [18]. According to Kirchhoff's law, at equilibrium, the emissivity of a material is equal to its absorptivity, at a given temperature. Therefore, by designing a material/structure to be highly absorptive over a prescribed wavelength range, one can argue that it is also a highly emissive mechanism over that selected wavelength range.

1.2 Focal Plane Array Applications

The second major application that was explored in this project was to utilize MTMs to enhance the performance of Focal Plane Arrays (FPA), and more specifically Infrared FPA (IRFPA) operating around near-IR wavelengths, 0.7-2.5 μm.

The problem at hand can be seen in Figure 1, which shows a high-level sketch of a sideview along one dimension of a 2D FPA (not to scale). An array of detectors is spaced out with a certain pixel pitch size, and each detector is positioned at the center of the pixel. Each detector is smaller than a pixel and therefore only covers part of the pixel. The beam from an objective lens is incident on the FPA and illuminates a spot on a pixel. If the beam spot hits any of the pixel detectors, the energy is absorbed in the detector to create electron-hole pairs in the active region leading to a photocurrent that can be sensed via read-out circuit. However the problem arises in the scenarios where the spot falls in the area of the pixels where there is no detector, and all or most power of the power is therefore lost, leading to lower quality image. This is the scenario that is relevant to the current focal-plane array development between DRDC/Valcartier and NRC. Therefore it is desired to devise a mechanism by which the spots falling outside the detectors are somehow still sensed, by the corresponding detector of the pixel the spot has fallen on.

From Lens or IR Lens

Hit   Miss

Detector

| 1 | 2 | 3 | 4 |
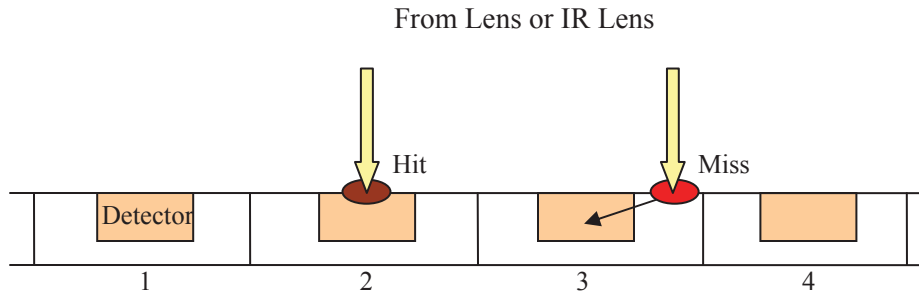
Figure 1. Array of spaced detectors in a FPA and incident spot beams from an objective lens. The spot beams hitting the detectors are absorbed, but the power of the spot beams falling in between detectors is lost.

1.3 Anisotropic Low Index Metamaterials

We use anisotropic metamaterials to refract and guide light for our purposes and intended applications. For optical and infrared applications, this type of metamaterials can be realized using periodic layers of metal and dielectric, inspired by the works done in [25]-[27] at microwaves and in [28]- [30] in the optical regime. We explore different configurations of these structures that potentially yield light collection, absorption, wave guidance, focusing, and narrow-band emission of light.

We primarily treat TM polarized light (in-plane electric field), which in the general case can exhibit different permittivity values along the two axes of the anisotropic uniaxial medium. The medium is assumed to be non-magnetic with μ=1. The material of interest has a permittivity tensor such as

$$\overset{=}{\varepsilon} = \begin{bmatrix} \varepsilon_{xx} & 0 & 0 \\ 0 & \varepsilon_{yy} & 0 \\ 0 & 0 & \varepsilon_{zz} \end{bmatrix}$$

The contrast between the permittivity of the two axes is what enables the desired guidance and focusing of light. The transverse permittivity is used to match the medium to the surrounding media, e.g. air, for normal incidence.

2 Guiding Power Along the Interface of Two Media

Consider Figure 2, where a TM plane wave is incident at a slightly off-normal angle on an anisotropic MTM surface with different longitudinal (z) and transverse (x) permittivity values. The MTM has close-to-zero permittivity along the longitudinal z-axis, $\varepsilon_{zz}=\pm0.1$, and is matched in the transverse direction $\varepsilon_{xx}=1$. Under these conditions, the incident light will refract such that the power flows almost parallel to the surface of the MTM. Such refraction and guidance of power is shown for both cases of $\varepsilon_{zz}=\pm0.1$ with the Poynting vector in Figure 3. Note that the refracted wave is not a "bound surface wave", instead is a free propagating wave in the lower half-space and can be further guided if needed. It can be seen that both positive and negative refraction can be achieved, depending on the sign used for the longitudinal permittivity of the MTM. From a dispersion standpoint, this means we can use either hyperbolic or elliptic dispersion, depending on the choice of the sign of the longitudinal permittivity.
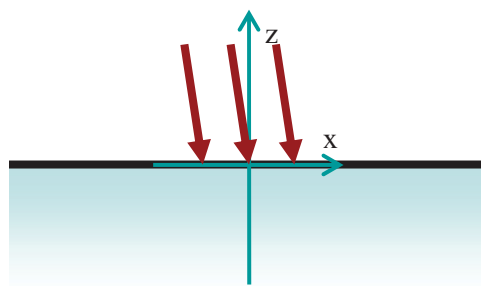
Figure 2. Off-normal light incident at the interface of air and an MTM with εzz=±0.1, εxx=1

This seemingly simple refraction is actually not encountered in nature and with dielectrics. Normal dielectrics in fact refract an incoming off-normal light closer to normal, as $\varepsilon_r>1$. The guiding capability shown here suggests that one can create higher transverse path length for the refracted wave. Therefore this can increase the chance of absorption of the incoming power. It suggests one can use a thinner material, as the longitudinal component of the ray path is much shorter than the transverse. This result can be useful for absorber/TPV applications.
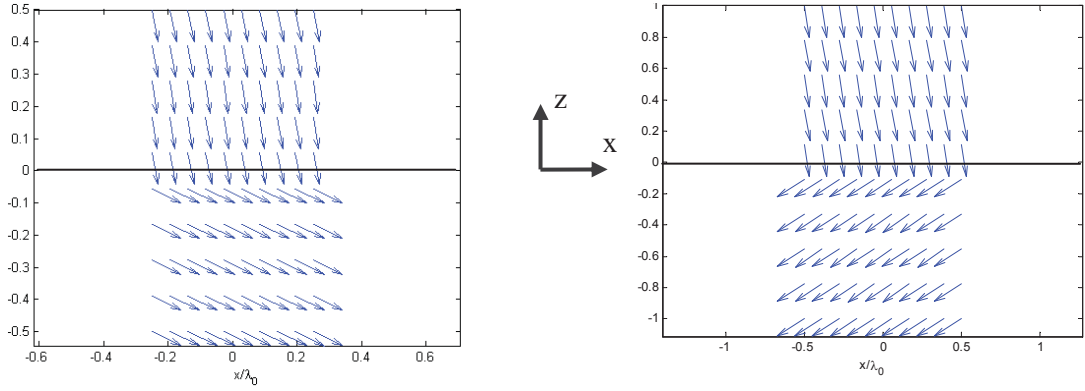
Figure 3. Power Flow showing refraction of an off-normal TM wave incident at the interface of an anisotropic MTM with low longitudinal permittivity (a) positive refraction with ε_{zz}=0.1, ε_{xx}=1, (b) negative refraction with ε_{xx}=1, ε_{zz}=-0.1

2.1 Reflection Analysis

The amount of reflection from the interface of the MTM for the two cases of interest is found by deriving the reflection coefficient formula. This is found by enforcing the boundary conditions for the tangential electric and magnetic fields at the interface. We find that

$$r_{pp} = \frac{\cos\theta\sqrt{\varepsilon_{xx}} - \sqrt{1 - \sin^2\theta / \varepsilon_{zz}}}{\cos\theta\sqrt{\varepsilon_{xx}} + \sqrt{1 - \sin^2\theta / \varepsilon_{zz}}}$$

Figure 4 shows the trend of the reflection coefficient from the interface of an anisotropic low permittivity MTM with ε_{zz}= +0.1, ε_{zz}=1, and compares it to the reflection from an isotropic MTM with ε_r= +0.1. The figure shows that the reflection is lower in our anisotropic case (black curve), for all angles below 15 degrees, than the isotropic slab of low permittivity (red curve). It also shows that the two slabs only accept plane waves that are incident up to a critical angle equal to $\sin^{-1}(\varepsilon_{zz})$. Beyond the critical angle, light going from air (dense medium) to the MTM slab experiences Total Internal Reflection (TIR) back into air. Hence this scenario is most useful for close to normal incidence.

5
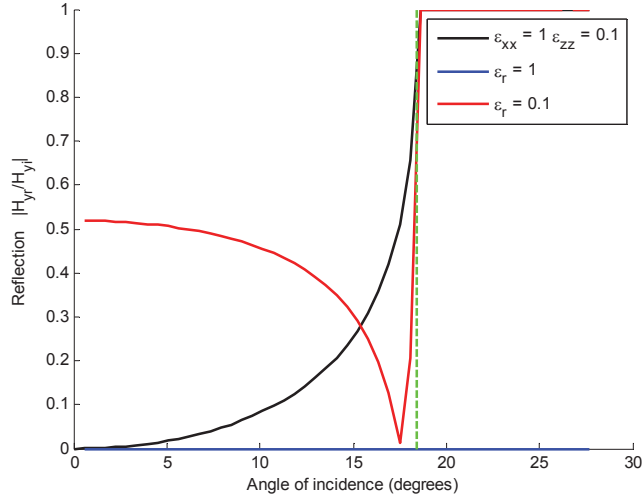
Figure 4. Reflection coefficient from the interface of air and anisotropic MTM with εxx=0.1, εzz= 1, and compared to the reflection from the isotropic MTM with εr = +0.1

Figure 5 shows the reflection coefficient at the interface of air and an anisotropic MTM with $\varepsilon_{zz}=$ -0.1, $\varepsilon_{xx}=1$, and also compares this to reflection from a dielectric such as typical glass. The results are verified with full-wave simulations (blue dots).

It can be seen that the reflection increases in an almost linear fashion with respect to the angle of incidence for this MTM. This implies that there is angle dependency on light collection, but the amount of reflection below a certain angle of incidence can be acceptable. It must be noted that the amount of reflected power is actually related to $|r|^2$, and is therefore a small fraction for most angles. There is no critical angle any more in this case, and the transmitted wave is propagating for any incident angle all the way to 90 degrees, as the MTM is now an "indefinite" medium. The MTM slab has lower reflections than glass for incident angles below 17 degrees, and performs worse than glass in terms of reflection for incident angles above 17 degrees. There also seems to be no Brewster angle (i.e. the angle at which reflection = 0) for the reflection from the MTM half-space, while glass has as Brewster angle at 56 degrees incident for TM polarized light.
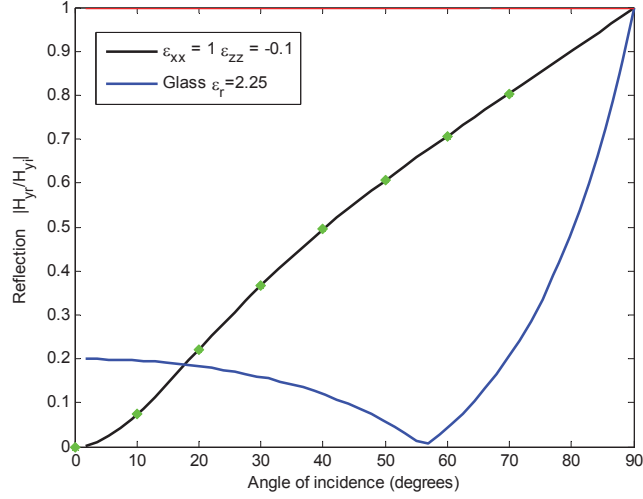
Figure 5. Reflection coefficient from the interface of air and anisotropic MTM with εxx= -0.1, εzz= 1, and compared to the reflection from glass εr = 2.25.

2.2 Rotated Crystal

The previously discussed concept can also be used to guide normal incident light, by rotating the crystal by a slight angle α in the x-z plane, as shown in Figure 6 (a). The rotation causes an inclined surface as shown. The same rotated crystal may also be cleaved along the x-axis, and it will still bend normal incident light with a large angle, and making it propagate along the interface as shown in Figure 6 (b). The permittivity tensor of the rotated crystal can be found by coordinate rotation, and using a rotation matrix R(α), where

$$R(\alpha) = \begin{bmatrix} \cos\alpha & 0 & -\sin\alpha \\ 0 & 0 & 0 \\ \sin\alpha & 0 & \cos\alpha \end{bmatrix}.$$

The final permittivity matrix of the rotated slab $\overline{\overline{\varepsilon}}'$ in the x-z coordinates is $\overline{\overline{\varepsilon}}' = R(-\alpha)\overline{\overline{\varepsilon}}R(\alpha)$

.

The power flow in Figure 7 confirms that a MTM half-space with such a rotated permittivity tensor indeed refracts the normal incident light in the same desired fashion.

7

<p align="center">(a)   (b)</p>
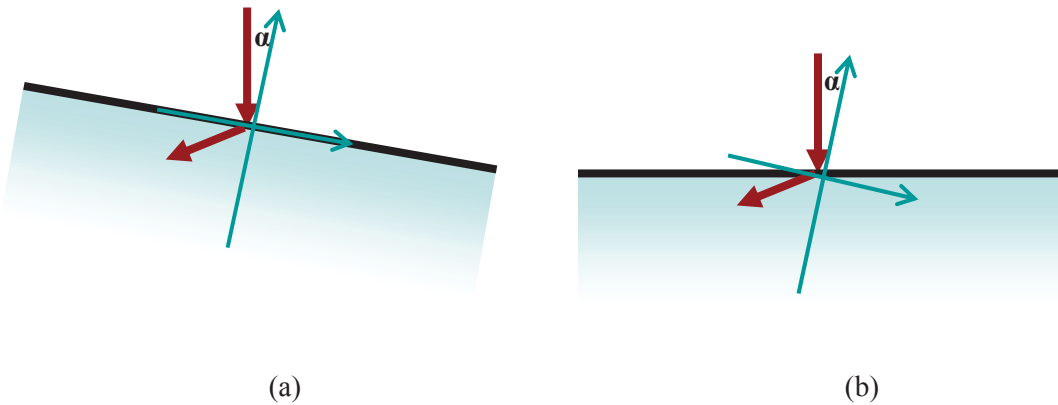
Figure 6. (a) Rotated crystal to guide normal incident light with an inclined interface, and (b) rotated crystal with a cleaved surface along the x-axis.

Poynting vector, $\phi = 0$, $\varepsilon_{11} = 0.96683$, $\varepsilon_{12} = -0.18811$, $\varepsilon_{21} = -0.18811$, $\varepsilon_{22} = -0.066831$
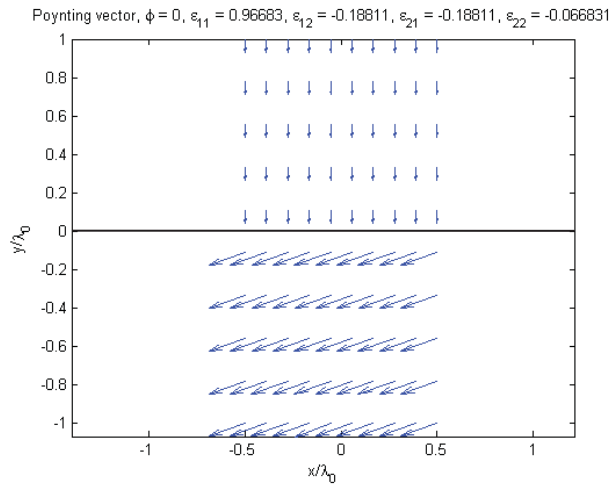
Figure 7. Power flow showing bending of normal incident light using a rotated and cleaved crystal.

3 Power Concentrator

Using the previous observations, we propose a structure that collects light over a larger area and guides it towards the center of the structure. Figure 8 proposes this structure which is a hetero-junction of two media, and concentrates incident power into a region in the middle of the structure, and is therefore termed a power concentrator.

<p align="center">8</p>

Each side of the junction uses the previously discussed medium with permittivity tensor components $\varepsilon_{xx}=1$ and $\varepsilon_{zz}=0.1$. We place two of such media side-by-side, and rotate the optical axis of the two sides by two opposite small angles $\pm\alpha$, giving rise to two inclined planes. As shown in Figure 8, the normal incident light refracts at the two inclined planes accordingly. The power is guided towards the center of the structure on each side, and an area of high power concentration is realized in the middle. The simulation results using a homogenized model are shown in Figure 9, showing both the field magnitude and power flow, and confirm the hypothesized operation.

This structure may potentially be useful both as an absorber or as an emitter for solar and TPV applications if tuned to the desired wavelength, as it creates a hot spot inside the structure. The concentrated energy/power can be absorbed to heat up the structure directly, or to heat up a secondary structure in contact with the hetero-junction.
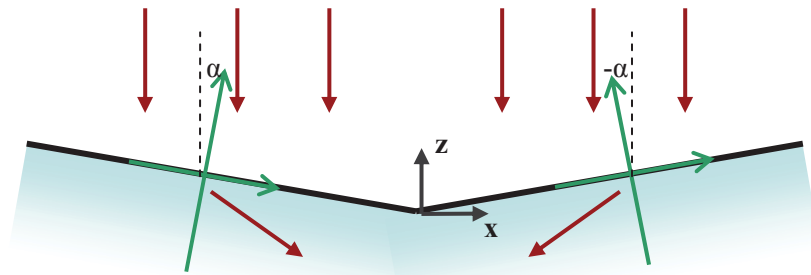
Figure 8. A power concentrator realized with two rotated anisotropic media

(a) (b)
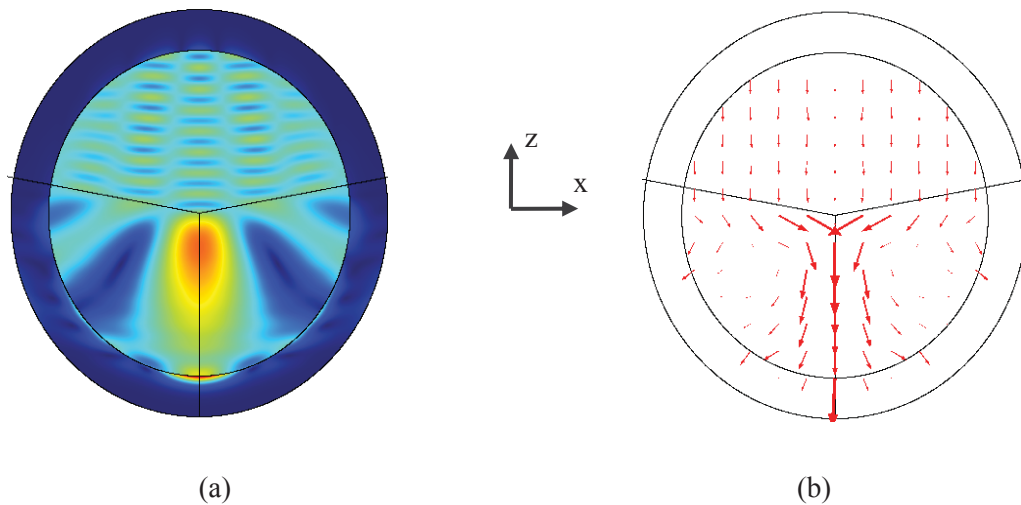
Figure 9. (a) Magnitude of H field homogenized model, (b) Power flow towards the center of the structure.

9

4 Focusing Device

The guiding capability of the proposed MTM hetero-junction can be utilized to create a compact low profile focusing device, in the order of several wavelengths at the operating frequency. The focusing device is depicted in basic form in Figure 10 (a) and Figure 11 (a). The device uses two adjacent slabs of crystals with oppositely rotated principal axes. The slabs of crystals are now finite, and the overall structure operates similarly to a lens. Each slab is a rotated and cleaved crystal, and guides the incident power towards the center of the structure similar to the power concentrator. But the addition is that light is transmitted through, and creates a spot of high power concentration at some distance away from the structure. This is a non-imaging lens, and can have applications in focusing power especially for FPA applications. The interface need not be cleaved, and can be kept at a slanted angle as was done in Figure 9. A cleaved surface along the x-axis would allow realizing very flat and low profile designs.

Figure 10 shows the operation (a) and simulation results (b) for a device made with two rotated crystals with hyperbolic dispersion, i.e. with a low negative-index along the longitudinal axis. This results in negative refraction at the top interface. A device using elliptical dispersion (low and positive index along the longitudinal axis) is also shown in Figure 11. It can be seen in both figures that an area of high field concentration is achieved.

To our knowledge this is the first time that a flat low-profile concentrator of light has been devised with the use of anisotropic MTMs. Also, in contrast to other designs where the field intensity is increased inside a medium, this design focuses the power in an external region similar to a lens. This is particularly useful for solar-concentration applications, where light with high concentration needs to shine the PV, and in particular for FPA/IRFPA applications, were light over a larger area should be focused into a smaller area.
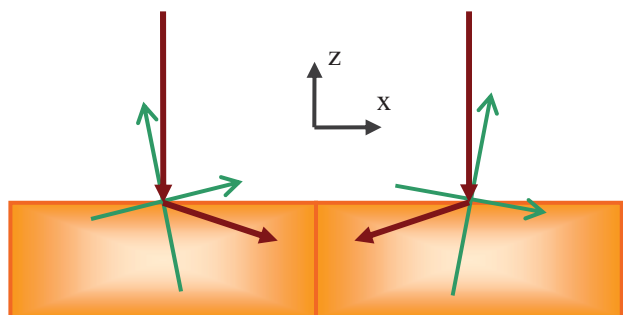
(a)
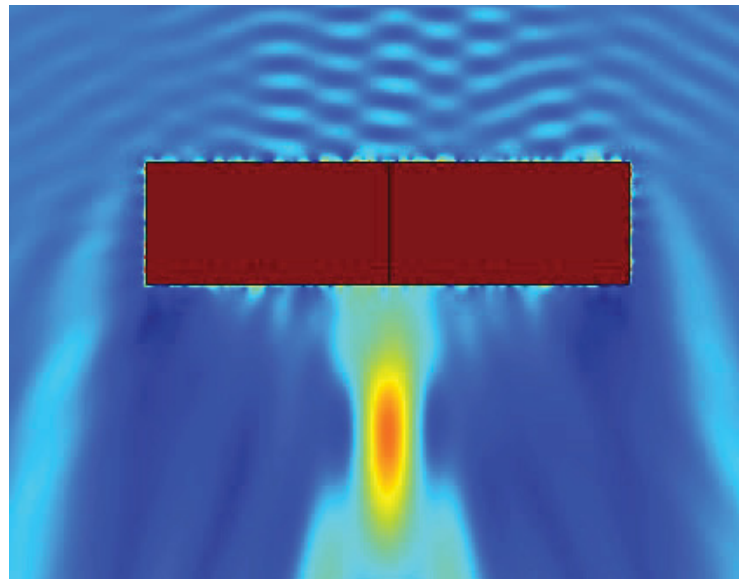
(b)

Figure 10. (a) A focusing mechanism / light concentrator realized with two adjacent rotated-axes anisotropic slabs guiding power to the center, using negative near-zero longitudinal permittivity. Simulated magnitude of H-field for TM light at normal incidence with a homogenized model.
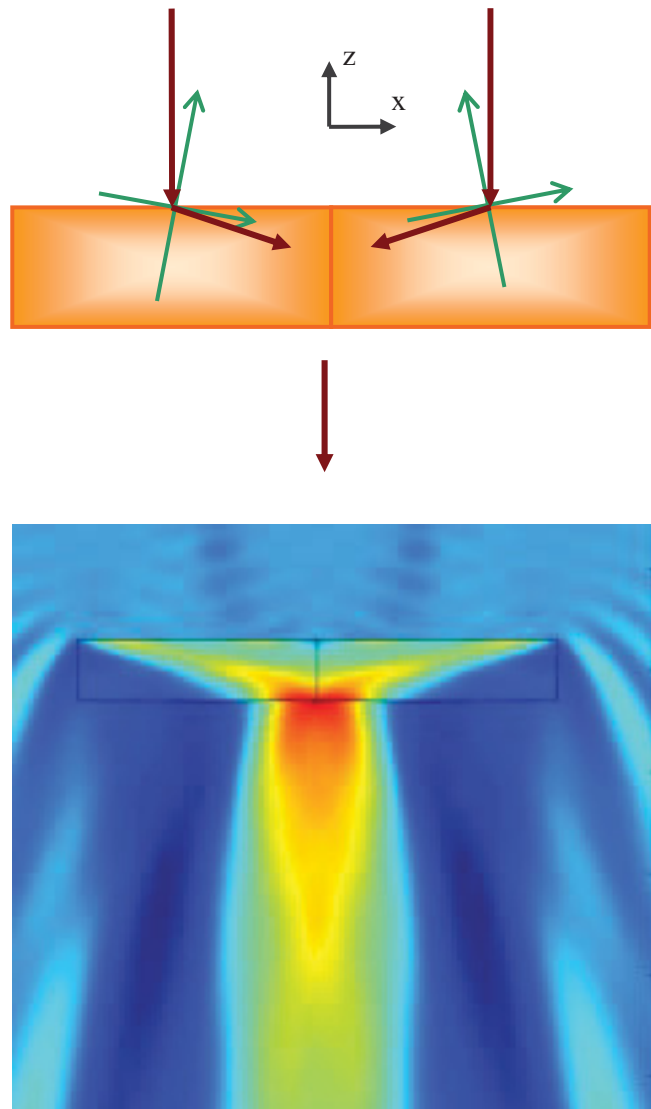
Figure 11. (a) A focusing mechanism / light concentrator realized with two adjacent rotated-axes anisotropic slabs guiding power to the center, using positive near-zero permittivity. Magnitude of H-field for TM light at normal incidence (b) homogenized model (c) stacked layer structure.

5 Periodic Bi-Layer Realization

In order to realize the aforementioned MTM devices at the optical and IR regimes, we use sub-wavelength periodic bi-layers of two materials, possibly a metal and a dielectric. Such a periodic bi-layer medium is known to yield an effective uni-axial crystal with a well defined optical axis [25]. Two orientations are possible for the optical axis as shown in Figure 12. Primarily, horizontal layers as in Figure 12 (b) have been used in the past [28]- [30], but we also investigate possibilities with vertical layers (Figure 12 (a)), wherever they may offer advantageous capabilities. The effective permittivity along the two principal axis can be found using the following first order Effective Medium Theory (EMT) formulas [25]:

$$\varepsilon_{axis} = \frac{\varepsilon_m \varepsilon_d}{(1-p)\varepsilon_m + p\varepsilon_d}$$

$$\varepsilon_{\perp axis} = p\varepsilon_m + (1-p)\varepsilon_d$$

where ε_m and ε_d are the permittivity of the metal and dielectric layers respectively and p is the filling ratio of the metal layer (thickness of the metal layer divided by sum of the thickness of metal and dielectric layers).
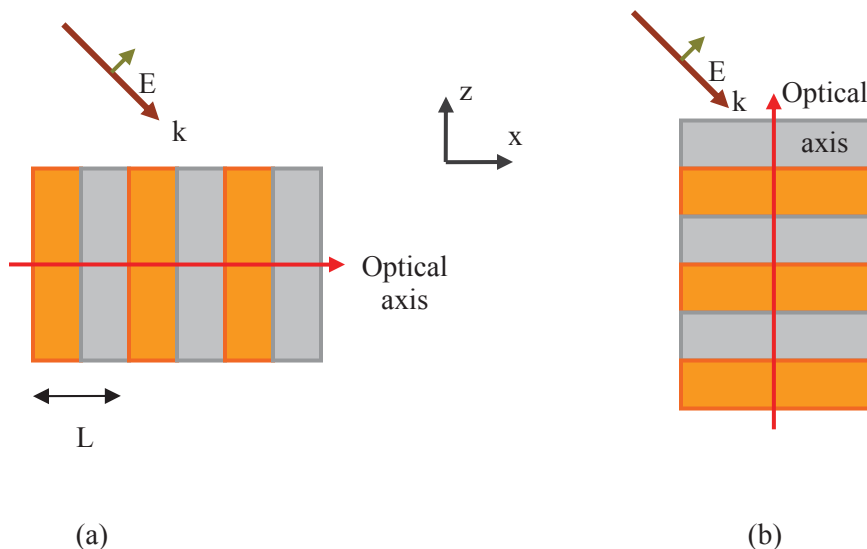
Figure 12. TM light incident on stacked periodic layers realizing an anisotropic medium with two different principal axes oriented along (a) x-axis and (b) z-axis.

5.1 Power Concentrator

We first try to realize the power concentrator previously discussed. It is found that layers of metal with $\varepsilon_m = 0.0513$, and a dielectric layer with $\varepsilon_d = 1.9487$, with a filling ratio of p=0.5 can yield the desired permittivity of 0.1 and 1 along the two axis. Figure 13 shows the full-wave simulation of the layered structure realization of the power concentrator based on these values, and compares it to the results previously obtained from the homogenized model. It can be seen that a close agreement exists between the two results.
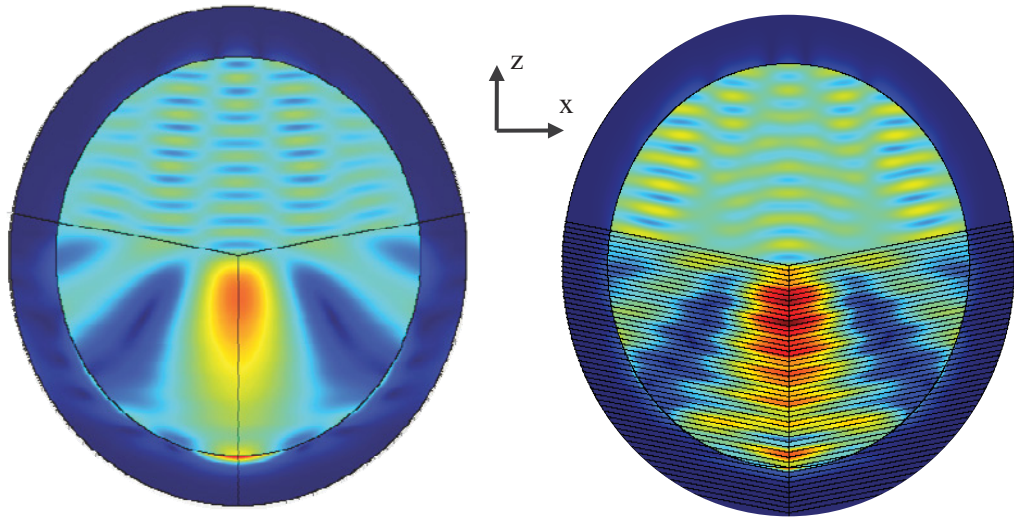
Figure 13. Power Concentrator realized with a horizontal bi-layer metal dielectric realization, for an unrotated permittivity of εxx = 1, εzz = 0.1.

This realization is a good first step, and is potentially possible at some frequencies given the choice of materials. However a more realistic design is desired in practice, which will be shown in the following section.

5.2 Focusing device

To synthesize more realistic designs, we have to include losses and use real materials with their corresponding permittivity at the wavelengths of interest. This approach is taken for the realization of the focusing device of Figure 10. Here we utilize bi-layers of silver (Ag) at λ_0=633nm having ε_m=-18+0.5*j for the metal layer, and Air ε_d=1 for the dielectric layer. Figure 14 shows the effective permittivity along the two major axis of this bi-layer structure for different

values of the filling ratio 'p'. The target values are found to be achieved for low filling ratios of the metal. A zoomed in version of the curve is shown in Figure 14 (b) around the operation point of interest. From the first order formulas it is found that the desired ratio is p=0.06.
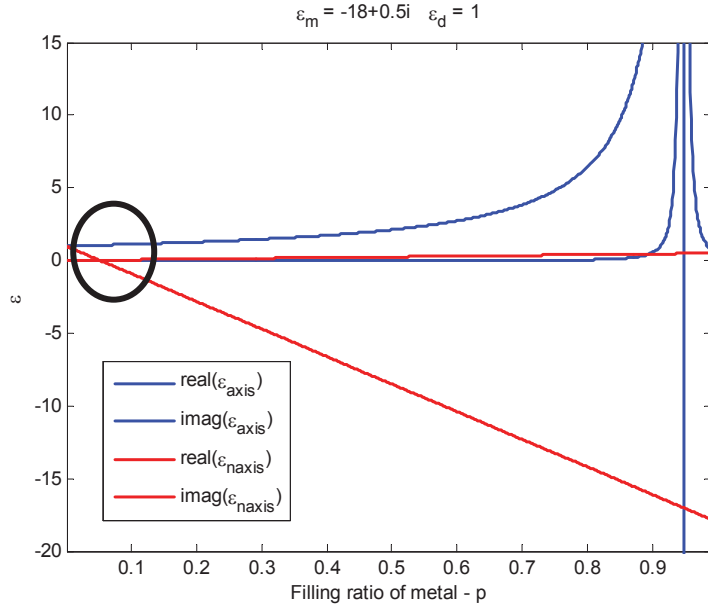
(a)
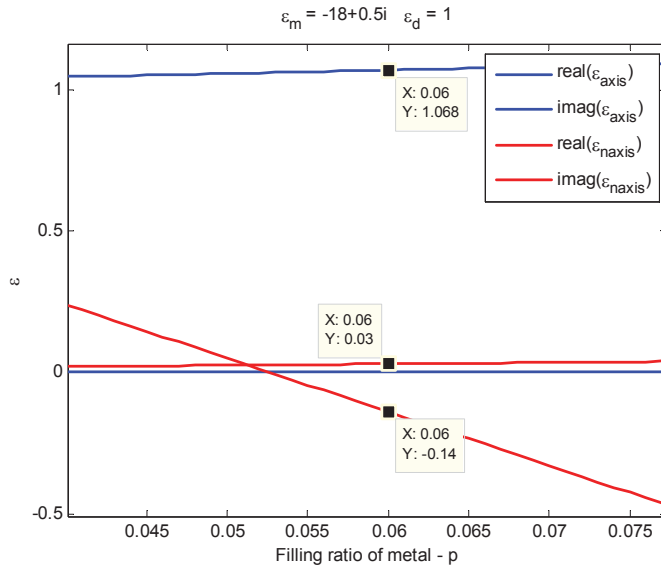
(b)

Figure 14. (a) Effective permittivity along the two axis as a function of filling ratio for layers of Ag and Air at 633nm and (b) a zoomed version of the graph around values of interest.

The focusing device slabs are then implemented with this bi-layer combination with a period of $L=\lambda_0/10$, and tilt angle $\alpha=\pm10°$. However initial simulations did not show the best focusing operation behavior and the design required optimization. By refining the design parameter p around the operating point it is found that a p=0.03 yields the desired behavior. The final simulation of the device is shown in Figure 15. It can be clearly seen that a distinct bright focus point is now achieved, with significant field enhancement at that point. This demonstrates a focusing device with realistic materials and having losses included, operating at 633nm.
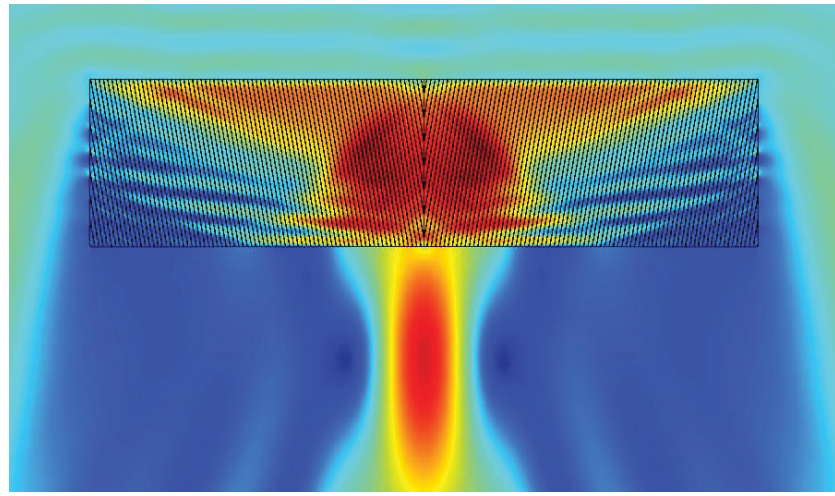
Figure 15. Magnitude of electric field from a focusing MTM device realized with layers of Ag and Air at λ0=633nm, under plane-wave illumination.

The power flow through this layered focusing device is shown in Figure 16. It can be clearly seen that the focusing device collects the incident normal power from the top surface and guides it towards the middle via refraction, and transmits a high concentration of power at the middle of the structure.
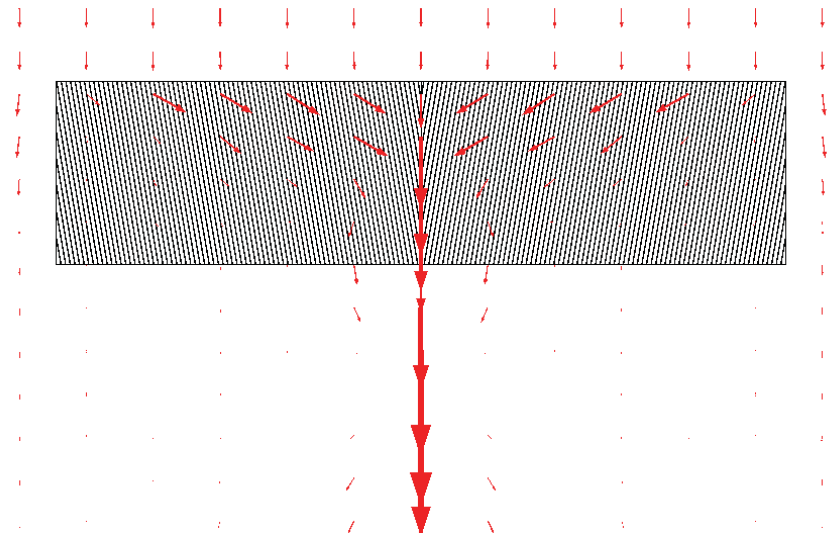
Figure 16. Power flow (Poynting vector) from focusing device realized with layers of Ag and Air at λ_0=633nm, under plane-wave illumination.

6 Array of MTM Hetero-junctions for FPA Applications

We can now utilize the proposed focusing device structure for the FPA array problem of interest.

6.1 Operation under Gaussian illumination

So far we have analyzed and investigated all designs with normally incident "plane waves". Since the light incident on the FPA is from a focusing lens, we now investigate the behaviour of the device under Gaussian beam illumination. Sample simulations of the focusing device with the homogenized model are shown in Figure 17, and the behaviour of the real lossy bi-layer design of Figure 15 is shown in Figure 18. It can be seen that a significant focusing is still achieved with Gaussian beam illumination.

(a)   (b)
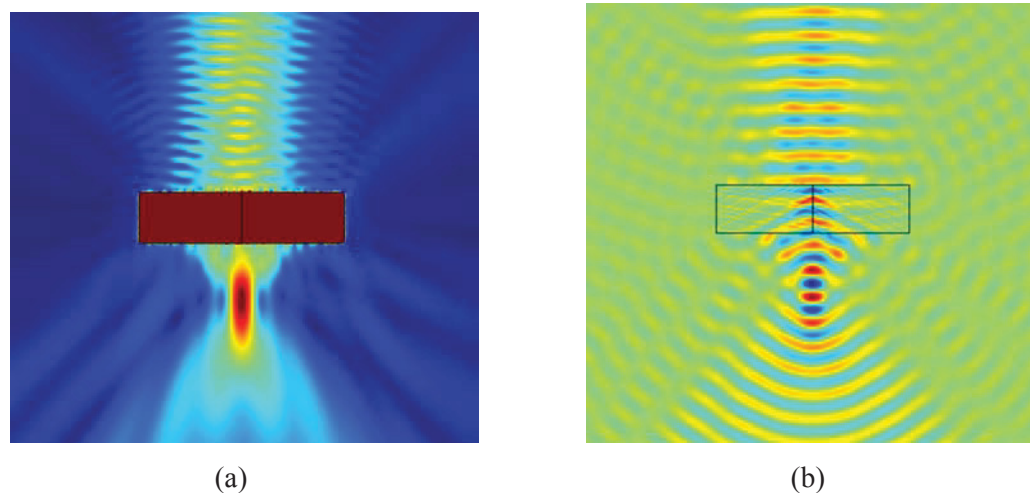
Figure 17. Focusing device under Gaussian beam illumination with homogenized model (a) magnitude of E field and (b) real part of E field.
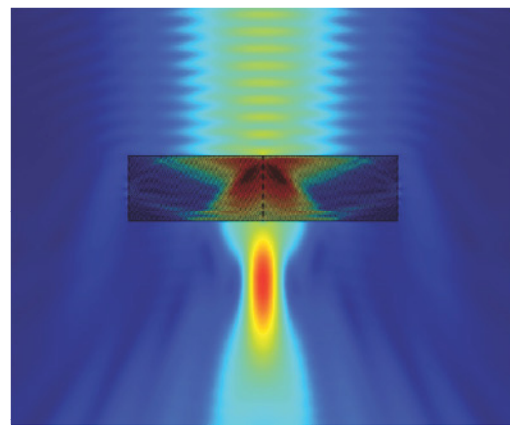
Figure 18. Gaussian beam illumination of the lossy bi-layer design of the focusing device.

6.2 Application to a Focal Plane Array

An array of the proposed focusing devices can be used in a FPA setting to address the problem described in 1.2. Consider adding a layer comprising an array of focusing devices on top of the FPA pixels as shown in Figure 19. Each focusing device spans one pixel and is situated such that its focus shines the pixel's detector. As shown in the figure, we expect now that each device guides any light falling on it towards its center, and focuses it on its focus spot.
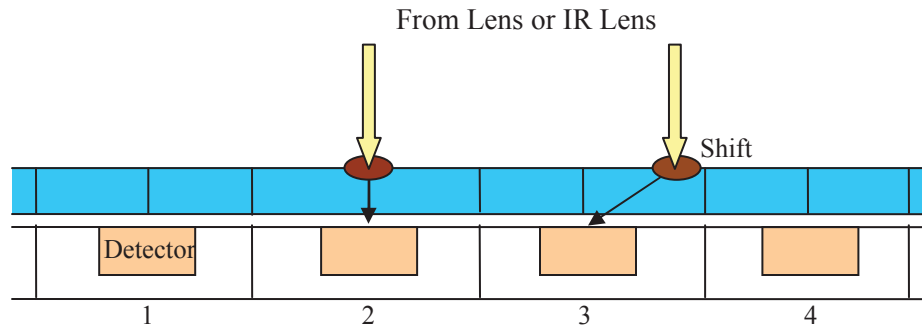
Figure 19. Array of focusing devices to direct light of a miss scenario to the corresponding pixel.

To test this hypothesis, a two element array is simulated under a Gaussian Beam illumination with a waist size of $\omega_0 = 2.5 \lambda_0$. The simulation results are shown in Figure 20. It can be clearly seen that as the incident beam moves laterally, the power is always directed by the focusing devices such that a focus develops on the detector of the corresponding pixel. Essentially the array of devices always locks the incident power of the beam to its corresponding pixel, and avoids any loss of power falling in between adjacent detectors.
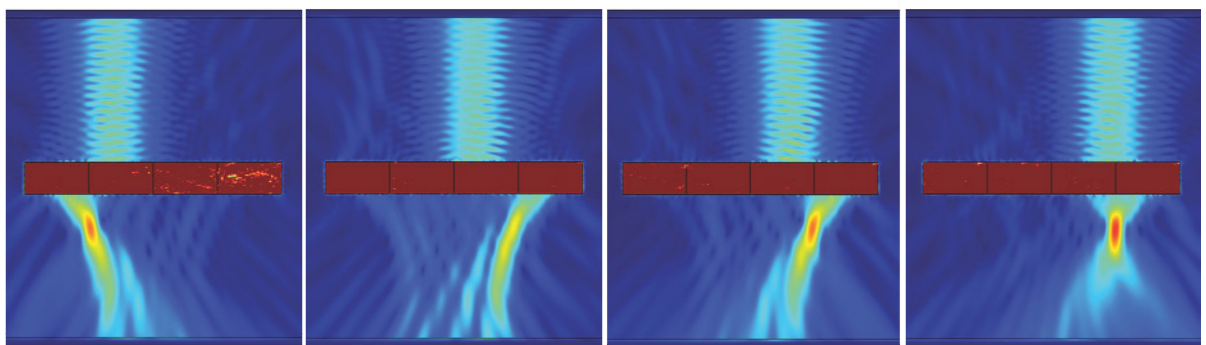
Figure 20. Gaussian beam illumination of an array of devices showing locking of power to corresponding pixels as the beam shifts laterally over the pixels.

In the worst case where a beam falls right on the middle of two focusing devices, Figure 21 shows that the power is split between two adjacent detectors. This power would have been otherwise completely lost in the absence of the focusing layer.
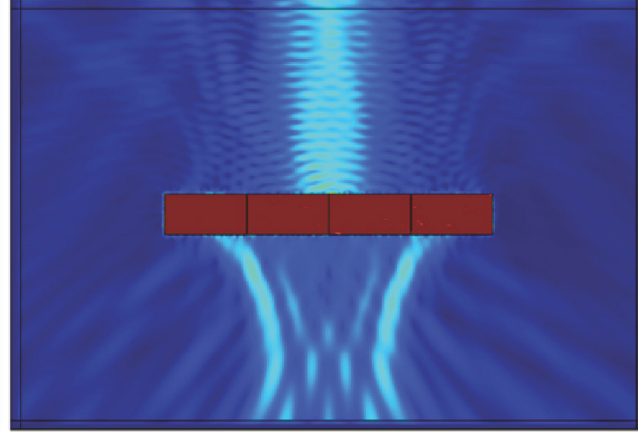
Figure 21. Worst case where the spot hits on the edge between two pixels, the power is equally split between two adjacent detectors and is still not lost.

In case of imperfect junctions, i.e. a junction with an air gap, Figure 22 shows that the device still can concentrate/guide the incident light towards a corresponding detector, again for different beam locations. This is an important benefit as it relaxes the fabrication requirements on having a perfect junction.
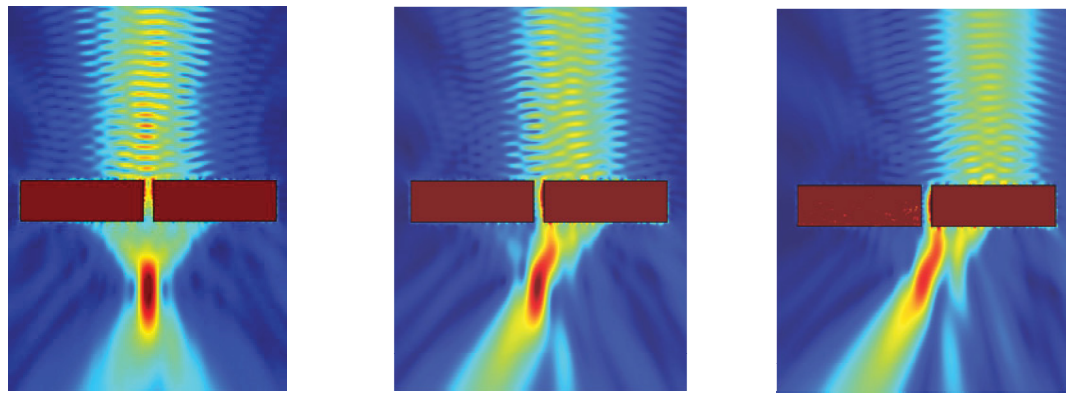
Figure 22. An imperfect junction with an air-gap under different lateral illumination still shows focusing capability.

The imperfect junction results also open the door for a second scenario of a focusing/guiding layer for the FPA problem as shown in Figure 23. Here a layer is added only in the distances

20

between consecutive detectors. We place one slab from each focusing device to shift the incident beams either to the left or right and guide the light to the corresponding detector. In this scenario, when there is a direct hit of the beam to a detector, the beam is collected directly and without any additional medium. The guiding/focusing only is used in the cases where a spot falls in between detectors and is guided accordingly.
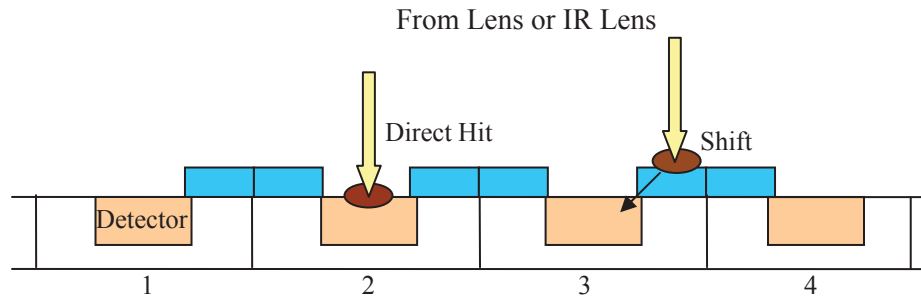
Figure 23. Array of beam guiding slabs filling the distance between detectors.

7 Radiation of Dipoles above and inside Low Index MTM

We have also investigated the radiation of antennas (whether at microwave or optical regimes) at the interface of the previously discussed MTM devices, and also propose ideas that are potentially useful for optical frequencies, which were not shown before. Some of the results presented in this section are published in [29].

A scenario of interest is shown in Figure 24, where the dipole is sitting at the interface of air and the low index MTM, which is potentially anisotropic. In [32] radiation pattern of dipoles at the interface of isotropic normal dielectrics ($\varepsilon_r = 4$) were found. The results of [32] showed interesting shaped radiation patterns inside the dielectric region, and it was noted that the radiation strength is much stronger in the dielectric than in the air side. We use a low-index MTM instead of the high permittivity dielectric, and then show that under such circumstances, those strong patterns become possible in air.
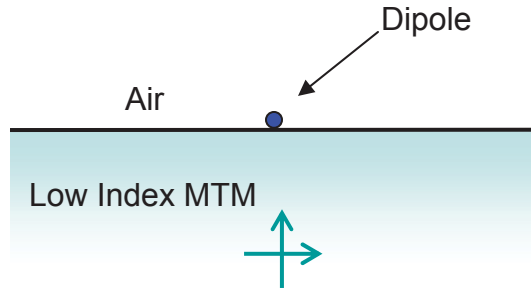
Figure 24. Dipole radiating above an anisotropic MTM.

7.1 Solution

The Lorentz reciprocity method is used to find the radiation pattern of the dipole above a general anisotropic MTM. This was also the method used in [32], but for the simpler case of isotropic medium and is extended here. The Lorentz method leads to the fact that the radiation pattern in air is the same as transmission coefficient (vs. angle) at the air-MTM interface. The problem coordinates are shown in Figure 25.
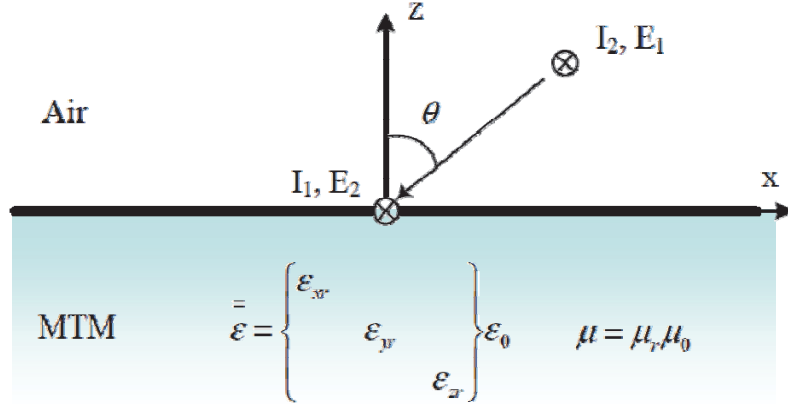
Figure 25. Dipole radiating above an anisotropic MTM.

By utilizing the reflection coefficient found in 2.1 and finding the transmission coefficient, we find the following expressions for the radiation patterns of the dipole above a uni-axial MTM interface.

$$S_{E-plane}(\theta) = \left[\frac{\cos\theta\sqrt{\mu_r - \sin^2\theta/\epsilon_{zr}}}{\cos\theta\sqrt{\epsilon_{xr}} + \sqrt{\mu_r - \sin^2\theta/\epsilon_{zr}}} \right]^2$$

$$S_{H-plane}(\theta) = \left[\frac{\mu_r\cos\theta}{\mu_r\cos\theta + \sqrt{\mu_r\epsilon_{yr} - \sin^2\theta}} \right]^2$$

7.2 Results

Figure 26 shows the plot of the derived expressions for the radiation pattern of a dipole at the interface of a low permittivity isotropic MTM with ϵ_r = 0.1. It can be seen that the interesting shaped radiation patterns of [32] are now achieved in the air side, instead of the dielectric as in [32], and the patterns are indeed stronger in air than in the MTM. This is a significant result, as the radiation patterns of [32] were required to be then somehow coupled into air, for instance by using a large spherical matching interface in the far-zone of the dipole-dielectric.

The observed effect is simple to understand with the following argument. By using the low permittivity MTM, the air is now playing the role of the dielectric in [32], and the interesting strong radiation patterns occur now in air.

23
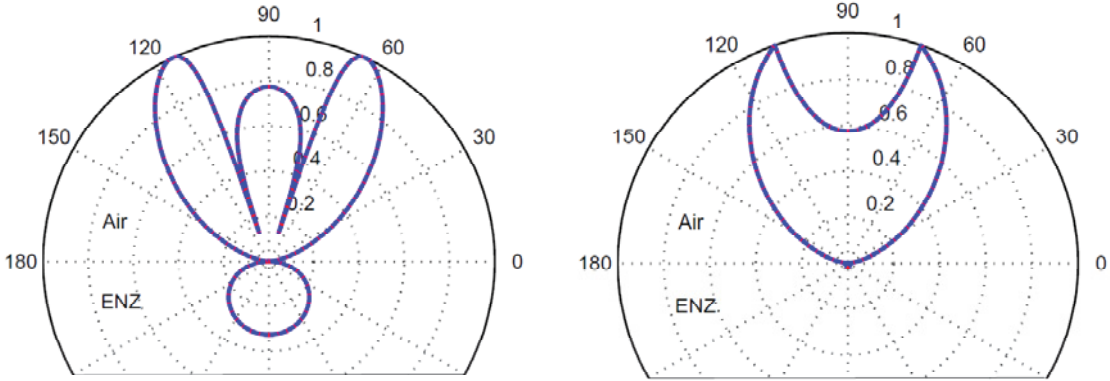
Figure 26. Dipole radiating above an anisotropic MTM.

Figure 27 shows the radiation pattern of the dipole at the interface of an anisotropic MTM with different values of low longitudinal ε_{zr}, and also compares it to the radiation pattern with the isotropic case. It can be seen that even with the more realistic model of anisotropic low index MTM, similar interesting shaped radiation patterns can be achieved in the air-side.
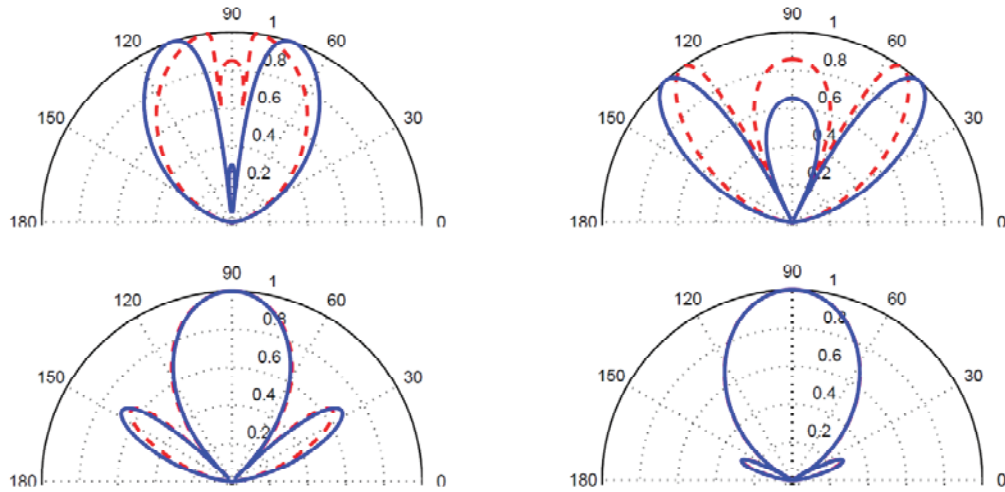
Figure 27. E-plane radiation pattern in air for a dipole above an anisotropic low ε MTM (solid blue curve). The MTM has $\varepsilon_{xr} = \varepsilon_{yr} = 1$ and (top-left) $\varepsilon_{zr} = 0.01$ (top-right) $\varepsilon_{zr} = 0.2$ (bottom-left) $\varepsilon_{zr} = 0.5$ (bottom-right) $\varepsilon_{zr} = 0.7$. Dashed red curve shows the corresponding isotropic MTM with $\varepsilon_r = \varepsilon_{zr}$.

7.3 Source inside an MTM hetero-junction

Several works up to now have proposed using MTMs for improving antenna radiation patterns. Most notably [31] proposed to embed a source in an isotropic low permittivity medium to achieve higher directive emission, and demonstrated this concept at microwaves with metal meshes realizing the MTM. A source was placed inside this isotropic low-index MTM of ε_r=0.1. Rays exiting the structure refracted close to normal in air, causing directive emission.

An interesting result can be obtained by embedding a radiator inside our proposed hetero-junction power concentrator discussed previously. Essentially we now use the power concentrator in transmit mode, and place the radiator at the hot spot of the received mode. The source is embedded λ_0 away from surface of hetero-junction. This scenario is compared with the scenario of a dipole embedded inside the low permittivity MTM [31], and the simulation results are shown in Figure 28.

(a)   (b)
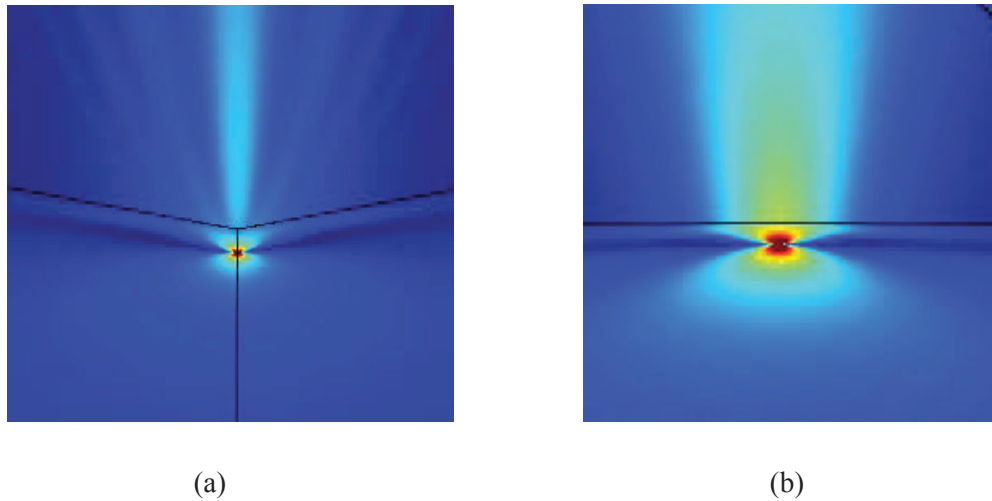
Figure 28. H field magnitude simulation of a horizontal dipole embedded inside the (a) power concentrator hetero-junction and (b) the MTM proposed in [31].

The far-field radiation pattern of these two cases are shown in Figure 29. It can be clearly seen that notably higher directive radiation is obtained by embedding the source inside the hetero-junction, compared to the proposition of [31].

This scenario not only provides better directive emission than [31] but it offers the important benefit that it can be extended to optical frequencies using real materials with a bi-layer design, which was not proposed with the design in [31], and has the potential for creating directive optical antennas. Potential applications include better coupling to sensors and emitters (e.g.

quantum dots, fluorescent molecules etc). The focusing device may also be used in the transmit mode for these intends and purposes.
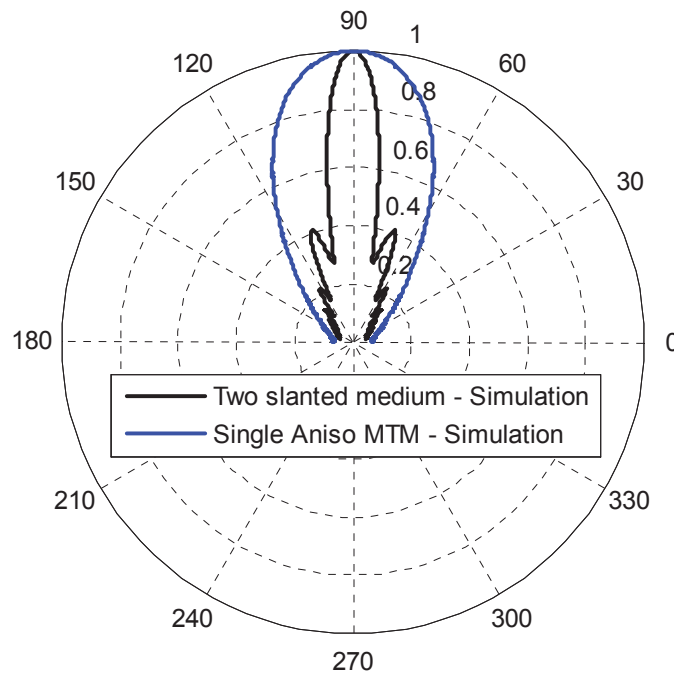
Figure 29. Far-field radiation pattern of a dipole embedded inside the power concentrator and compared to the anisotropic scenario of [31].

Conclusions

The proposed low permittivity anisotropic media are versatile in realizing various designs and metamaterial structures for seemingly very different applications. The range of applications can include solar and thermo photovoltaics, imaging photo-detectors, focal plane imaging arrays (FPA)s, infrared FPAs, Concentrated Photovoltaics, directive emission, optical antennae, etc. Various design using hetero-junctions of rotated anisotropic media where proposed, namely the power concentrator, the focusing device, two focusing device layers for FPA enhancement, a radiator on MTM surface, and a radiator inside a power concentrator. Structures with real lossy materials were also presented and characterized. The presented ideas, designs and structures can have significant impact on the aforementioned applications, and therefore are good candidates for further development and evaluation, and ultimately fabrication and testing together with photodetectors.

References

[1] J. Karp, "Concentrating Solar Power: Progress and Trends," Presentation at University of California San Diego, Feb 2009.

[2] Y. Cui, K. H. Fung, J. Xu, H. Ma, Y. Jin, S. He, and N. X. Fang "Ultrabroadband Light Absorption by a Sawtooth Anisotropic Metamaterial Slab," Nano Letters 12, pp. 1443-1447, Feb. 2012.

[3] Y. Avitzour, Y. A. Urzhumov, and G. Shvets, "Wide-angle infrared absorber based on a negative-index plasmonic metamaterial," *Phys. Rev. B 79(4),* 045131, Jan. 2009.

[4] E. Rephaeli and S. Fan, "Tungsten black absorber for solar light with wide angular operation range," *Appl. Phys. Lett.* 92(21), 211107, 2008.

[5] N. P. Sergeant, M. Agrawal, and P. Peumans, "High performance solar-selective absorbers using coated sub-wavelength gratings," *Opt. Express*, 18(6), pp. 5525–5540 Mar. 2010.

[6] C. Wu, Y. Avitzour, and G. Shvets, "Ultra-thin, wide-angle perfect absorber for infrared frequencies," *Proc. SPIE, Proceedings of Metamaterials: Fundamentals and Applications*, San Diego, CA, August 10–14 (2008).

[7] Y. Cui, K. Fung, J. Xu, S. He, and N. Fang, "Multiband plasmonic absorber based on transverse phase resonances," Opt. Express 20, 17552-17559, 2012.

[8] J. Hao, Jing Wang, X. Liu, W. J. Padilla, L. Zhou, and M. Qiu, "High performance optical absorber based on a plasmonic metamaterial," Appl. Phys. Lett. 96, 251104 2010.

[9] X. Liu, T. Tyler, T. Starr, A. F. Starr, N. M. Jokerst, and W. J. Padilla, "Taming the blackbody with infrared metamaterials as selective thermal emitters," *Phys. Rev. Lett.* 107(4), 045901 (2011).

[10] J. A. Mason, S. Smith, and D. Wasserman, "Strong absorption and selective thermal emission from midinfrared metamaterials," *Appl. Phys. Lett.*, 98(24), 241105, Jun. 2011.

[11] L.-G. Wang, G.-X. Li, and S.-Y. Zhu, "Thermal emission from layered structures containing a negative-zeropositive index metamaterial," *Phys. Rev. B 81(7)*, 073105, Feb. 2010.

[12] Bermel P, et al. "Tailoring photonic metamaterial resonances for thermal radiation," *Nanoscale Res Lett,* 6:549, 2011.

[13] E. Nefzaoui, J. Drevillon, and K. Joulain, "Selective emitters design and optimization for thermophotovoltaic applications," *J. Appl. Phys.* 111, 084316, Apr. 2012.

[14] N. Mattiucci, G. D'Aguanno, A. Alu, C. Argyropoulos, J. V. Foreman, and M. J. Bloemer, "Taming the thermal emissivity of metals: A metamaterial approach," *Appl. Phys. Lett.* 100, 201109, 2012.

[15] C. Wu, B. Neuner III, G. Shvets, J. John, A. Milder, B. Zollars, and S. Savoy, "Large-area wide-angle spectrally selective plasmonic absorber," *Phys. Rev. B,* 84(7), 075102, 2011.

[16] G. D'Aguanno, N. Mattiucci, A. Alù, C. Argyropoulos, J. Foreman, and M. Bloemer, "Thermal emission from a metamaterial wire medium slab," Opt. Express 20, 9784-9789 (2012).

[17] W. Spirkl and H. Ries, "Solar thermophotovoltaics: an assessment," *J. Appl. Phys.* 57, pp. 4409–4414, 1985.

[18] C. Wu, B. Neuner, J. John, A. Milder, B. Zollars, S. Savoy and G. Shvets, "Metamaterial-based integrated plasmonic absorber/emitter for solar thermo-photovoltaic systems," *J. Opt.14*, 024005, Jan. 2012.

[19] E. Rephaeli, and S. Fan, "Absorber and emitter for solar thermophotovoltaic systems to achieve efficiency exceeding the Shockley-Queisser limit," *Opt. Express* 17, pp. 15,145–15,159, Aug. 2009.

[20] M. Rahm, D. Schurig, D. A. Roberts, S. A. Cummer, D. R. Smith, J. B. Pendry, "Design of electromagnetic cloaks and concentrators using form-invariant coordinate transformations of Maxwell's equations," Photonics and Nanostructures - Fundamentals and Applications, Volume 6, Issue 1, Pages 87-95, April 2008.

[21] W. Wang, L. Lin, J. Ma, C. Wang, J. Cui, C. Du, and X. Luo, "Electromagnetic concentrators with reduced material parameters based on coordinate transformation," *Opt. Express* 16, 11431-11437 (2008).

[22] S. Das, "Metamaterial Integrated Solar Concentrator," US Patent, US 2012/0067419 A1, Sep 14, 2011.

[23] J. Yang, M. Huang, C. Yang, Z. Xiao, and J. Peng, "Metamaterial electromagnetic concentrators with arbitrary geometries*," Opt. Express 17*, 19656-19661 2009.

[24] W. Shockley and H. J. Queisser, "Detailed Balance Limit of Efficiency of p-n Junction Solar Cells," *J. Appl. Phys.*, 32, 510, 1961.

[25] R.E. Collin, "A Simple Artificial Anisotropic Dielectric Medium," *IRE Trans Microw. Theory Tech*, vol.6, no.2, pp.206-209, Apr. 1958.

[26] K. G. Balmain, A. A. E. Luttgen, and P. C. Kremer, "Resonance cone formation, reflection, refraction and focusing in a planar anisotropic metamaterial", *IEEE Antennas Wireless Propagat. Lett.*, vol. 1, pp.146 -149 2002.

[27] G.V. Eleftheriades, O. F. Siddiqui, "Negative refraction and focusing in hyperbolic transmission-line periodic grids," *Microwave Theory and Techniques, IEEE Transactions on* , vol.53, no.1, pp.396,403, Jan. 2005.

[28] Z. Jacob, L. Alekseyev, and E. Narimanov, "Optical Hyperlens: Far-field imaging beyond the diffraction limit," *Opt. Express 14*, pp. 8247-8256, Aug. 2006.

[29] Z. Liu, H. Lee, Y. Xiong, C. Sun and X. Zhang, "Far-Field Optical Hyperlens Magnifying Sub-Diffraction-Limited Objects," Science 23, Vol. 315, no. 5819, pp. 1686, March 2007.

[30] A. Salandrino and N. Engheta, "Far-field subdiffraction optical microscopy using metamaterial crystals: Theory and simulations," Physical Review B (Condensed Matter and Materials Physics), vol. 74, no. 7, Aug. 2006.

[31] M. Memarian, G. V. Elefhteriades, "Radiation of Dipoles at the interface of anisotropic low permittivity media," IEEE AP-URSI Conf., Jul. 2013.

[32] D. Rutledge and M. Muha, "Imaging antenna arrays," *Antennas and Propagation, IEEE Transactions on*, vol. 30, no. 4, pp. 535 – 540, Jul. 1982.

[33] S. Enoch, G. Tayeb, P. Sabouroux, N. Guérin, and P. Vincent, "A metamaterial for directive emission," *Phys. Rev. Lett.* 89(21), 213902, 2002.